

Design Studies of Thin-Haul Commuter Aircraft with Distributed Electric Propulsion

Alex M. Stoll*, Gregor Veble Mikić†

Joby Aviation, Santa Cruz, California, 95060

A conceptual design study of a distributed electric propulsion transport aircraft is presented. The objective is to study the applicability of distributed electric propulsion configurations to aircraft serving thin-haul airline routes. A series hybrid powertrain is selected, such that shorter routes can be operated on battery power alone, while longer routes can be operated with a range extender, to reduce the required battery size. Two range extender options are examined: a modern turbodiesel and an advanced recuperated turbogenerator. Conventional fuel-powered aircraft are designed in parallel with the same mission and constraints, to illustrate the relative impact of the electric propulsion configurations on the chosen metrics. An operating cost model is assumed, to assess the commercial viability of the various designs. The advanced concepts are generated and analyzed using purpose-built conceptual design tools, with optimization employed to minimize a weighted average operating cost of a short battery-powered flight and a longer hybrid-powered flight. The analysis tools are also used to model existing aircraft for comparison. Plots of various trade studies are presented. The results suggest that the configurations examined in this study present an advantage in operating costs over conventional aircraft, in addition to assumed noise and emissions advantages.

Nomenclature

A	Propeller disk area
A_u	Propeller disk area less obscured area
AR	Wing aspect ratio
AR_j	Aspect ratio of blown wing segment
b	Wingspan
C_D	Drag coefficient
C_T	Propeller thrust coefficient
C_{D_0}	Zero-lift drag coefficient
$C_{D_{cool}}$	Engine cooling drag
C_{D_i}	Lift-dependent drag
$C_{L_{max}}$	Maximum lift coefficient
d_m	Motor diameter
d_p	Propeller diameter
e	Span efficiency
e_0	Oswald efficiency
J	Propeller advance ratio
M	Propeller figure of merit
m_{wing}	Mass of the wing
M_s	Propeller figure of merit, not including swirl losses
N_z	Ultimate load factor

*Aeronautical Engineer, 340 Woodpecker Ridge, AIAA Member.

†Chief Aerodynamicist, 340 Woodpecker Ridge, AIAA Member.

Copyright © 2016 by Joby Aviation, LLC. Published by the American Institute of Aeronautics and Astronautics, Inc. with permission.

P_{\min}	Minimum engine size
P_{shaft}	Shaft power
P_A	Available power
$P_{A,0}$	Available power below critical altitude
Q	Motor torque (maximum continuous)
q	Freestream dynamic pressure
S	Wing planform area
S_{wet}	Wing wetted area
S_b	Wing blown planform area
T	Thrust
t/c	Wing average thickness-to-chord ratio
V_{∞}	Freestream velocity
V_{100}	Cruise speed for the 100 nm flight
V_{400}	Cruise speed for the 400 nm flight
V_{S0}	Stall speed in landing configuration
V_S	Stall speed (in the current configuration)
W	Maximum takeoff weight
w_f	Fuselage width

Symbols

η	Propeller efficiency
Λ	Wing quarter-chord sweep angle
λ	Wing taper ratio
λ_j	Aspect ratio of elliptical slipstream
ρ	Freestream air density
ρ_0	Air density at critical altitude
ρ_{wing}	Density of wing structure resisting bending
σ	Ratio of slipstream to freestream velocity
σ_{allow}	Allowable stress of wing structure resisting bending

I. Introduction

Recent advances in electric propulsion technology have enabled the design of vehicles that improve on conventional fuel-powered vehicles in many aspects—chiefly, operating costs, emissions, and noise. Whereas these benefits are extremely relevant to commercial aircraft, battery technology has generally limited electric vehicles to much shorter range than equivalent fuel-powered vehicles. However, this limitation may not be significant to the growing commercial aviation market serving the large number of low-demand routes. Such routes are referred to as “thin haul” and are typically characterized by shorter lengths and the use of relatively small aircraft, such as the ten-seat Cessna 402.

To assess the competitiveness of electric aircraft in this market, three configurations were studied and compared: a modern conventional aircraft and two different distributed electric propulsion configurations. All three designs use the same fuselage geometry so that passenger accommodation is consistent. These three designs were then compared to existing aircraft.

II. Background

The thin haul markets are currently served by aircraft such as the Cessna 402 and Pilatus PC-12, and the Tecnam P2012 will be introduced soon. The first three columns of table 1 list relevant specifications of these aircraft, and the cabin cross-sections are illustrated in figure 1. However, none of these aircraft are optimized for the thin haul market. Their range capabilities are excessive: for example, 67% of the flights of Cape Air, the largest commuter airline in the United States, are shorter than 100 nm, and all are shorter than 225 nm¹ (see figure 2), which is far shorter than the maximum range capabilities of these aircraft. Additionally, the relatively short takeoff and landing capabilities of the P2012 and PC-12 are not particularly beneficial in this market. Therefore, it can be expected that designing an aircraft specifically for this mission could result in a much more suitable aircraft.

Table 1. Aircraft specifications

	Cessna 402C ²⁻⁴	Tecnam P2012 ^{4,5}	Pilatus PC-12 ⁶	Advanced concepts
Range	875 nm	620 nm	1,845 nm	400 nm
Stall speed (V_{S0} , CAS)	67 knot	60 knot	67 knot	67 knot
Takeoff run	1,763 ft	1,410 ft	1,480 ft	2,000 ft
Seats	10	11	11	11
Cabin width	1.42 m	1.48 m	1.52 m	1.48 m
Fuselage length	10.0 m	11.7 m	13.3 m	11.7 m
Engine(s)	TSIO-520	TEO-540	PT6A	Varies
Total power	650 hp	700 hp	1,200 hp	Varies
Retractable gear	✓		✓	✓
Max cruise speed	194 KTAS	210 KTAS	285 KTAS	180-325 KTAS
Pressurized			✓	Varies
Year of introduction	1967	2019*	1994	2025
Construction	Aluminum	Aluminum	Aluminum	Carbon fiber composite

* Estimated

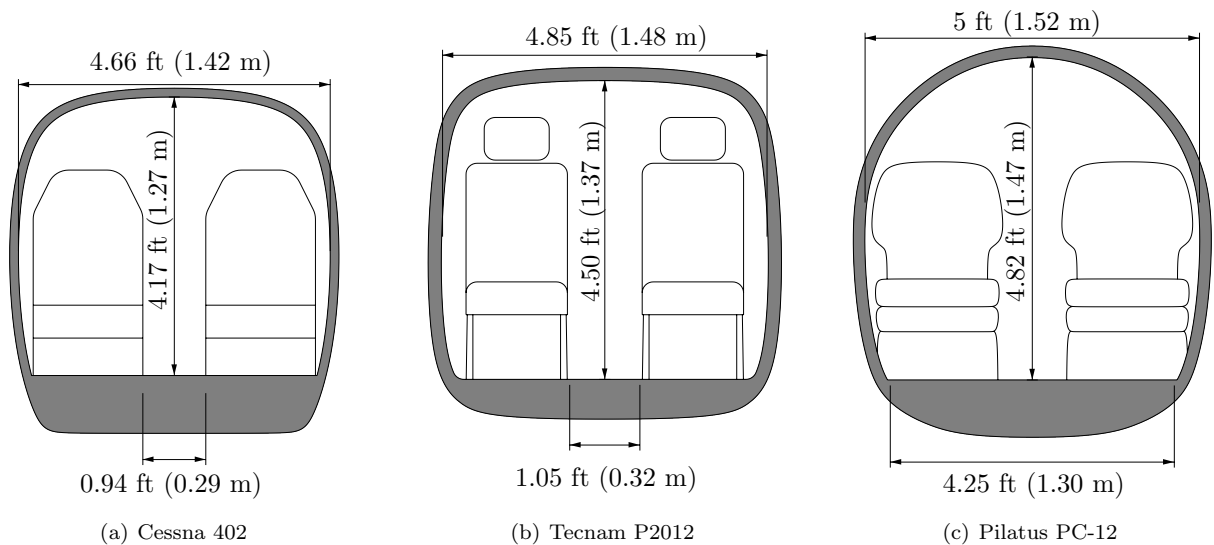


Figure 1. Cabin cross-sections of the reference aircraft

Electric propulsion provides many benefits relative to combustion-powered aircraft. Inherent to the configuration are benefits of reduced energy costs, maintenance costs, emissions, and noise. Additionally, electric motors are small and light relative to equivalent combustion engines, and they scale down without a prohibitive loss in specific power or efficiency;⁷ as a result, distributed propulsion configurations are significantly more practical with electric motors. A number of promising distributed electric propulsion concepts are considered in this study:

- A wingtip propeller installation can improve propulsive efficiency due to the favorable aerodynamic interaction between the wing and the propeller.⁸
- A series of small propellers mounted spanwise along the wing that blow the wing during takeoff and landing can allow the wing area to be reduced for a given stall speed,⁹ reducing cruise drag and improving ride quality. These propellers are fixed-pitch and fold flush against their nacelles during other phases of flight to reduce drag.
- A propeller mounted at the tip of the vertical tail can provide additional thrust during takeoff and climb and ameliorate yaw trim issues potentially arising from a wingtip propeller configuration in the event of a single wingtip motor or propeller failure. The tail installation reduces scrubbing drag relative to a conventional fuselage installation. This propeller is fixed-pitch and also folds flush against its nacelle during other phases of flight.

Although an electric aircraft powered only by batteries most capitalizes on the operating cost, noise, and emissions benefits of electric propulsion, it also is most hampered by range limitations. Therefore, the electric propulsion designs considered herein employ a hybrid architecture, in which shorter range missions can be completed solely on battery power, but a range extender is present for use for reserves or for longer-range missions.

Specifications chosen for the advanced concepts are also outlined in table 1. The Tecnam P2012's cabin dimensions (see figure 1(b)) and layout are adopted, under the assumption that they reflect contemporary market preferences. The level of electric propulsion technology (e.g., specific power of the motors, controllers, and batteries) is concordant with an intended entry into service in the year 2025. A variety of powerplant and cruise speed options are considered. Keeping with contemporary aircraft structural trends, carbon fiber composite construction was selected to reduce weight and maintenance costs.

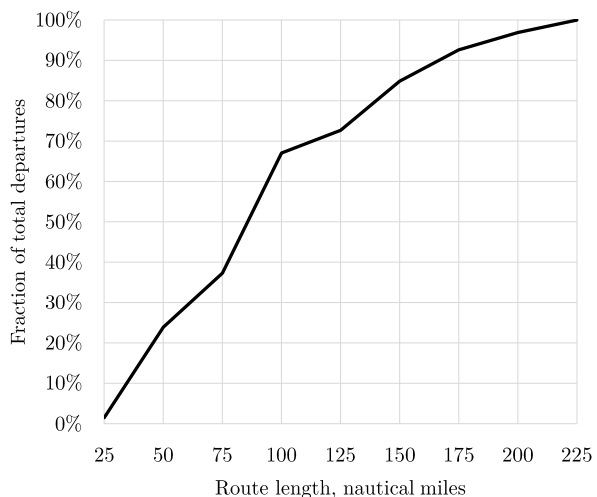


Figure 2. Cumulative histogram of Cape Air's 2016 scheduled commuter land routes (from Ref. 1)

III. Design Criteria

Based on the route profile of Cape Air and similar airlines, two missions were selected: a 400 nm flight and a 100 nm flight. The electric aircraft designs perform the 100 nm flight on battery power alone, but employ a generator as a range extender for the 400 nm flight. The cruise speed for the 400 nm flight, referred to as V_{400} , was varied from 180 KTAS to 325 KTAS to evaluate the impact of this parameter on other metrics, with the 100 nm flight flown at the most economical speed. Both the 400 nm and 100 nm flights are accompanied by a 67 nm IFR reserve.

The mission profile is illustrated in figure 3. The mission distance is the sum of mission segments 2, 3, and 4, and the alternate distance is the sum of reserves segments C, D, and E. Origin, destination, and alternate are at sea level, and all atmospheric conditions are ISA. Approach is conducted at a 3° glide slope from 3,000 ft to sea level at $1.3V_S$, where V_S is the stall speed at the respective configuration (i.e., in this case, the approach configuration). Climb and descent rates are 1,000 ft/min and 700 ft/min (5.1 m/s and

3.6 m/s), respectively. Descent speeds are equal to the cruise speed for the mission portion and $1.3V_S$ for the alternate portion. Climb speeds are equal to $1.3V_S$, except in the case of the mission climb segment (mission segment 2), in which the climb speed is a design variable.

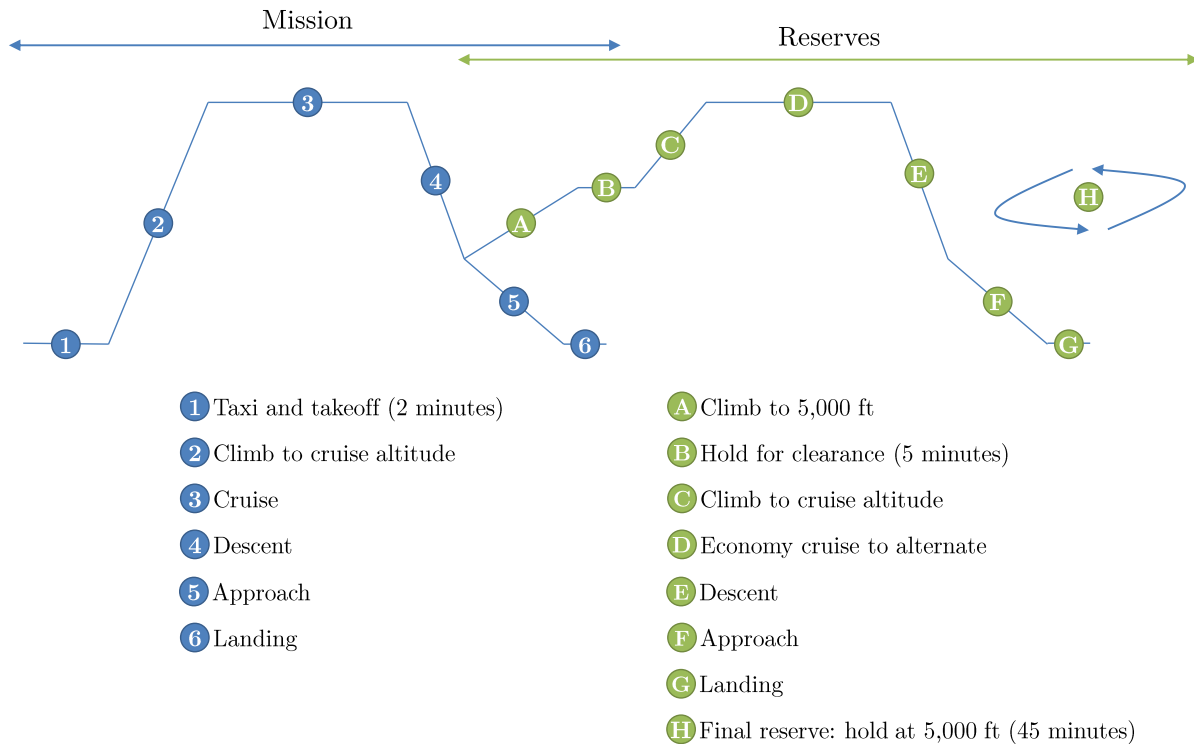


Figure 3. Design mission and reserve profile

The cruise altitude for the 100 nm mission is set to 8,000 feet (or 10,000 feet if the cruise speed is over 250 KEAS, due to Federal Aviation Administration restrictions specified by 14 CFR §91.117¹⁰). The cruise altitude for the 400 nm flight is a design variable, but pressurization (to a cabin altitude of 8,000 feet) is employed if this altitude is greater than 10,000 feet. Pressurization incurs weight and cost penalties according to the weight and cost models employed. (When analyzing the reference aircraft for comparison, all flights were completed at 8,000 feet, except for the Pilatus PC-12 which cruised at 25,000 ft for its 400 nm flight.)

A payload of 2,400 lb including pilot (based on Cape Air's preferences¹) was specified for the 100 nm mission; the maximum payload is allowed to decrease for the 400 nm flight, to allow for a greater weight of fuel to be carried.

Limit and ultimate load factors of 3.5 and 5.25, respectively, were selected.

While a low wing was selected for the conventional design, a high wing was selected for the electric designs to provide adequate clearance for the wingtip propellers in crosswind landings, where the aircraft roll angle can be significant. To further the goal of reducing wing area to improve energy efficiency, Fowler flaps, with a maximum extension of 40° , are employed from the wing root to 78% of span, with the outer 22% occupied by ailerons. Based on comparisons to similar configurations, this configuration is expected to achieve an unblown $C_{L_{max}}$ of 2.6 at 40° . A clean $C_{L_{max}}$ of 1.5 is assumed, along with a takeoff flap setting of 20° corresponding to an intermediate $C_{L_{max}}$ of 2.05. Wing taper was set to 0.6 as a compromise between structural efficiency and stall behavior, and no wing sweep is employed.

A conventional tail was selected for the conventional design, but the electric designs employ a T-tail, to reduce the chance of the propwash from the high-lift propellers causing unfavorable interactions with the horizontal tail. The tail sizes were determined by the tail volume method, where the greater of the tail volumes of the Cessna 402 and the tail volume coefficients calculated by the method of Morris and Ashford¹¹ (which accounts for the effect of the fuselage) was used. The vertical tail planform area may be increased from this size to meet motor-out trim constraints. Tail geometry parameters (taper, aspect ratio,

and sweep) were matched to those of the Tecnam P2012, except for configurations employing a T-tail, in which the vertical tail aspect ratio and taper were altered to more typical T-tail values of 0.8 and 0.95, respectively.

A longitudinal static margin of 25% was specified, with the assumption that the battery packs can be installed in a location allowing the requisite center of gravity to be achieved in a typical loading scenario. With the horizontal tail sized as described above, this dictates the location of the center of gravity which affects motor-loss trim considerations, described later.

Rubber engine sizing was employed, and a small number of engine families were defined to provide parameters such as specific power and specific fuel consumption. A modern turbodiesel was considered for both the conventional design and as a range extender for the electric designs. Alternatively, a conventional turboprop was considered for the conventional aircraft, and an advanced recuperated turbine was considered as a range extender for the electric aircraft. For safety, the conventional aircraft was designed to as a twin, with engines conventionally mounted on the wing. Similarly, the electric designs employ two cruise propellers, but due to the high reliability of the battery system, only a single range extender engine is required.

The three configurations chosen to be analyzed, and the associated abbreviated names, are:

- Conventional (C): modern combustion-powered design similar in layout to the Cessna 402
- Three-motor (3M): electric with range extender, employing wingtip propellers and a tail propeller
- High-lift propellers (HLP): electric with range extender, employing wingtip propellers and high-lift propellers to allow for increased wing loading

These three configurations are illustrated in figure 4. The high-lift propellers eliminate the need for a tail propeller to meet motor-out trim constraints.

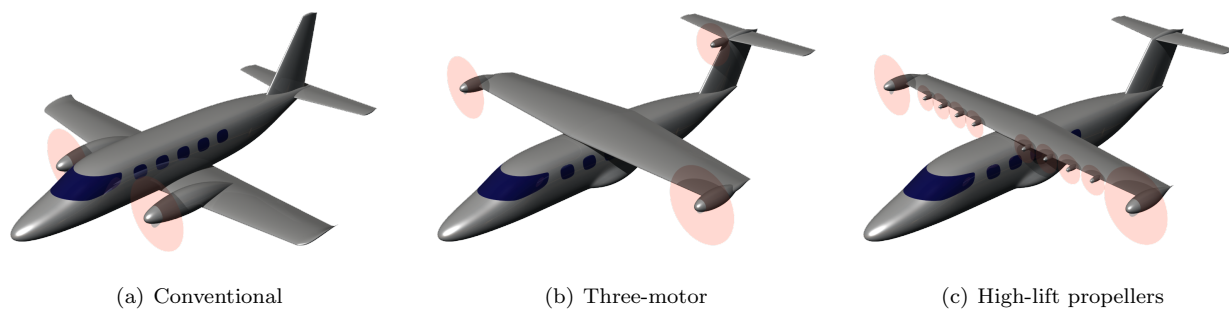


Figure 4. Illustrations of the advanced concept configurations

IV. Design and Analysis Methods

Aerodynamic, weight, performance, and cost models were integrated to create a purpose-build conceptual design and analysis tool. With the specification of design variables such as maximum takeoff weight and cruise speeds, the component weights and required fuel and battery weights for the given missions were found, allowing the resulting maximum payload weight for each mission to be determined. With a choice of objective, optimization was performed with a constraint placed on this resultant payload weight to ensure adequate payload. The generalized reduced gradient optimization algorithm was employed. The design variables and constraints (where applicable) are summarized in table 2.

Various optimization objectives were considered. Objectives such as minimizing maximum takeoff weight (MTOW) or the sum of the cost of electricity, battery amortization, and fuel for a given mission can be estimated with reasonable confidence, but the optimal designs for such objectives may not be reasonable. Therefore, a total operating cost metric was considered. Total operating cost is much more difficult to accurately predict, due to the inability to confidently estimate operating cost components such as maintenance costs and purchase costs at this point in the design stage of a new configuration; however, selecting this metric as the optimization objective produces very reasonable designs, and it was assumed that optimizing to an attempted estimate at total operating cost would still be more useful than optimizing to a metric

Table 2. Design variables

Variable	Minimum	Maximum
Maximum takeoff weight		
Wing area		
Wing aspect ratio		15
Wing average airfoil thickness	12%	18%
Climb speed	$1.3V_S$	250 KEAS*
V_{100} (100 nm flight cruise speed)	180 KTAS	
Cruise altitude, 400 nm flight	8,000 ft [†]	25,000 ft
Generator power	P_{min}^{\ddagger}	
Motor diameters		
Number of high-lift propellers	6	12

* When below 10,000 ft, per 14 CFR §91.117 (assuming IAS = EAS)

[†] For the $V_{400} = 325$ knot designs, the minimum cruise altitude was 10,000 ft.

[‡] P_{min} is the minimum possible engine size and depends on the choice of engine type.

that may be more realistically determined, but less relevant. Optimal designs for these three metrics are illustrated in figure 5. The lowest battery+electricity cost design exhibits features that reduce drag at the expense of weight, such as a high-aspect ratio wing and small-diameter motors. (Motor weight is inversely proportional to motor diameter.) In contrast, the lowest weight design exhibits features that reduce weight at the expense of drag, such as large-diameter motors. The lowest total operating cost design is a more practical compromise between the two.

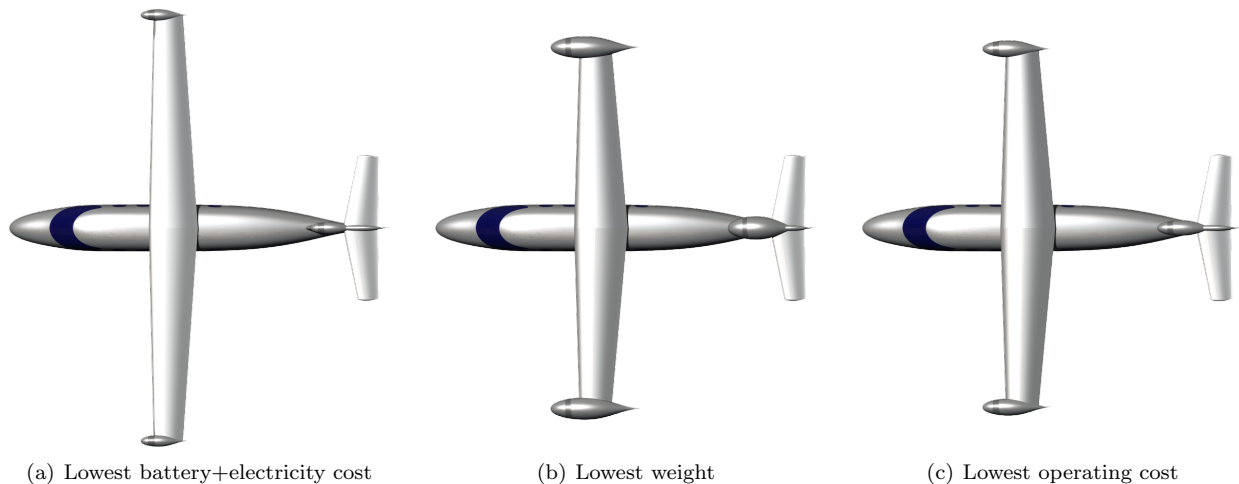


Figure 5. Comparison of optimization objectives

Based on the assumption that these aircraft will be operated in a range of mission lengths, the objective was chosen to be a weighted combination of the operating costs of the two design missions: 75% of the cost per nautical mile for the 100 nm flight, and 25% of the cost per nautical mile for the 400 nm flight.

The same analysis tool was also employed to estimate the performance and operating costs of three reference aircraft—the Cessna 402, Tecnam P2012, and Pilatus PC-12—for the same missions, to provide points of comparison with the advanced concepts.

A. Aerodynamic Models

The drag is modeled as $C_D = C_{D_0} + C_{D_i} + C_{D_{cool}}$, where the lift-dependent drag term C_{D_i} is given as

$$C_{D_i} = \frac{C_L^2}{\pi e_0 AR} \quad (1)$$

e_0 is the Oswald efficiency and C_{D_0} is fixed (aside from the contribution from extended landing gear, which is only present in applicable flight segments). $C_{D_{cool}}$ is the engine cooling drag.

1. Oswald and Span Efficiency

Span efficiency is estimated by a statistical model:¹²

$$e = 0.99 \left[1 - 0.0407 \left(\frac{w_f}{b} \right) - 1.792 \left(\frac{w_f}{b} \right)^2 \right] \quad (2)$$

The induced drag coefficient is then given by $C_L^2 / \pi e AR$.

The Oswald efficiency estimate is based off a statistical model,¹³ but adjusted to vary with e relative to an assumed typical value of e :

$$e_0 = k_{Oswald} [1.78(1 - 0.045AR^{0.68}) - 0.64] \frac{e}{(0.99)(0.975)} \quad (3)$$

Additionally, the adjustment factor k_{Oswald} was added to account for the effect of the nacelles and propellers on lift-dependent drag, and was chosen as 0.83 for mid-span-mounted engines (as on the Cessna 402 and Tecnam P2012) and 1.0 otherwise, based on fits to published performance data.^{2,6,14}

If the wing high-lift propellers are operating, the Oswald efficiency is assumed to drop to 0.5 (based off of blown wing CFD analyses) due to the suboptimal lift distribution.

2. Profile Drag

For the fuselage, wing, tails, and nacelles, the profile drag was calculated using the form factor method given by Kroo,¹² evaluated at the cruise condition of the 100 nm flight. The exception is the nacelle form factors, which are first calculated by the method proposed by Raymer;¹⁵ the form factor for the wingtip nacelles is then increased by 12%, to account for scrubbing drag, and the form factor of nacelles with folding propellers is increased by 29%, based on CFD simulations of nacelles with and without nested folded propellers¹⁶ (see figure 6).

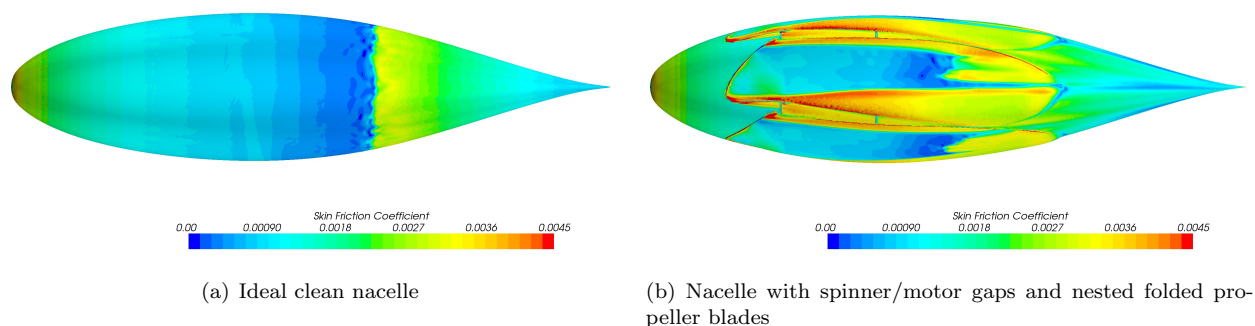


Figure 6. CFD simulations of nacelles in a cruise condition, utilizing a turbulent transition model

Wing wetted area is estimated as

$$S_{wet} = 2(1 + 0.2t/c)S \left(1 - \frac{w_f}{b} \frac{2}{1 + \lambda} \right) \quad (4)$$

Laminar flow assumptions are given in table 3.

An interference drag allowance of 4% is added to the profile drag of the vertical and horizontal tails, based off the suggestions given by Raymer.¹⁵

Table 3. Laminar flow assumptions

Component	Surface area fraction
Wing	30% less area in propwash
Tails	30%
Fuselage	5%
Cruise propeller nacelle	1%*
Other nacelles	40%†

* The flow behind the propeller is assumed turbulent, resulting in this low value.

† The estimated amount for a nacelle with folded propellers, based off of CFD studies (see figure 6).

Excrescence drag is included as a fixed drag area of 0.045 m².

Extended landing gear is assumed to have a drag area of 0.2 m²(W/13300 N), and is included only in the approach mission segments and applicable one-motor-inoperative conditions.

Flap drag (both parasitic drag and additional lift-dependent drag) is estimated with the models proposed by Raymer,¹⁵ assuming a flap chord of 30% and span of the exposed wing less 22% span (for ailerons).

For high-wing aircraft, the fuselage wetted area figure used for drag calculations was increased by 0.9 m² to account for the main landing gear fairings. (This does not apply to the P2012, since its gear is fixed.)

3. Cooling Drag

A simple engine cooling drag model is employed such that $C_{D_{cool}} = k_{cool}(C_{D_0} + C_{D_i})P_{engine}/P_{max}$, where P_{max} is the maximum power requirement of the design mission. Therefore, the cooling drag coefficient is at a maximum of $k_{cool}(C_{D_0} + C_{D_i})$ if the engine is sized to produce the entire power requirement of the aircraft, and an equivalent hybrid aircraft with the same P_{max} and an engine sized to, e.g., only half this power will experience half the cooling drag. A value of 7.5% was used for k_{cool} . For the hybrid aircraft designs, a retractable engine intake (as on the North American AJ Savage) is assumed, and so the engine cooling drag is included only when the engine is running.

Electric motor cooling drag is assumed to be an additional 0.25% of total drag per motor, and is bookkept in C_{D_0} .

4. Propeller Performance

The performance of the cruise propellers (i.e., the wingtip propellers on the electric propulsion concepts, and the wing- or nose-mounted propellers on the conventional concepts) was modeled by applying a figure of merit, M , to the ideal momentum theory model of the power required to produce a given thrust, ignoring swirl losses:

$$P_{shaft} = \frac{TV_{\infty}}{M} \frac{1}{2} \left(1 + \sqrt{1 + \frac{T}{qA_u}} \right) \quad (5)$$

A_u is the disk area less the area obscured by a fuselage (for a nose-mounted tractor propeller) or nacelle, to account for blockage effects.

Due to the potential for the high-lift propellers to reach high thrust coefficients, swirl losses cannot be neglected, so in this case, a model including approximate swirl losses¹⁷ was employed:

$$P_{shaft} = \frac{TV_{\infty}}{M_s} \left(\left[\frac{1}{2} + \sqrt{\frac{1}{4} + \frac{\pi^2}{4J^2} \left(1 - \sqrt{1 - \frac{16C_T}{\pi^3}} \right)} \right]^{-1} - \frac{J^2}{\pi^2} \left[\sqrt{1 + \frac{\pi^2}{J^2} \left(1 - \sqrt{1 - \frac{16C_T}{\pi^3}} \right)} - 1 \right] \right)^{-1} \quad (6)$$

Here, the figure of merit is referred to as M_s to indicate the explicit calculation of swirl losses.

Because the tail propeller operates in a narrow range of flight conditions, a simple efficiency model $P_{\text{shaft}} = TV_{\infty}/\eta$ was used.

A propulsive efficiency increase may be derived from locating propellers on the wingtips.⁸ To account for this effect, the shaft power requirement of wingtip propellers was scaled by the ratio of total drag less a fixed fraction of the induced drag to total drag. Based on CFD studies, this fixed fraction was chosen as 34%. The effect of this model is that designs with relatively high span loading flying at relatively low speeds will derive the most benefit from this configuration.

The diameters of the high-lift propellers are determined by the combination of two design variables: the number of high-lift propellers and the blown span percentage. The diameters of the other propellers are determined by the relation given by Raymer,¹⁵ $d_p = \sqrt[4]{(0.058 \text{ m}^4/\text{kW})P}$, where P is the maximum continuous power of the propeller.

Propeller parameters are given in table 4. Tip speeds are kept relatively low to reduce noise.

Table 4. Propeller parameters

Propeller	Efficiency	Tip speed (ft/s)
Cruise	$M = 89\%$	700 ft/s
Tail	$\eta = 85\%$	500 ft/s
High-lift	$M_s = 90\%$	450 ft/s

5. Blown Wing Performance

To estimate the increase in $C_{L_{\text{max}}}$ of the blown wing, a theoretical model of a wing in an elliptic slipstream¹⁸ was applied in a modified form, such that the blown portion of each side of the wing was analyzed as if it were immersed in an elliptic slipstream of the aspect ratio of a box bounding the respective series of high-lift propellers. This aspect ratio is referred to as λ_j . The ratio of the blown to the unblown lift curve slope was then calculated for these blown portions, and the ratio of lift curve slopes for the entire wing was assumed to be the ratio of the blown portions scaled by the ratio of blown wing area, S_b , to total wing area, S . The ratio of blown to unblown $C_{L_{\text{max}}}$ of the wing was then assumed to be equal to the ratio of blown to unblown lift curve slope of the wing, and is given by

$$\frac{C_{L_{\text{max,blown}}}}{C_{L_{\text{max,unblown}}}} = k_{\text{blow}} \left(\frac{C_{L_{\text{max,blown}}}}{C_{L_{\text{max,unblown}}}} \right)_j \frac{S_b}{S} + \left(1 - \frac{S_b}{S} \right) \quad (7)$$

where

$$\left(\frac{C_{L_{\text{max,blown}}}}{C_{L_{\text{max,unblown}}}} \right)_j = \frac{AR_j + 2}{AR_j + 2 \frac{1 + \sigma^2 \lambda_j}{\sigma^2 + \lambda_j}} \sigma^2 \quad (8)$$

is the $C_{L_{\text{max}}}$ ratio of the blown section, AR_j is the aspect ratio of each blown wing segment, and σ is ratio of slipstream to freestream velocity. k_{blow} is a simple statistical correction factor based on CFD analysis of a variety of blown wing configurations (see e.g. figure 7) and is given by

$$k_{\text{blow}} = 0.302 \frac{S_b}{S} + 0.792 \quad (9)$$

Although many simplifying assumptions are present in this model (e.g., wake contraction is negligible and the velocity in the slipstream is uniform), inclusion of the statistical correction factor modifies the model to describe the range of CFD results with little error.

Assuming axial flow, momentum theory gives $\sigma^2 = 1 + T/qA$, so the required thrust to blow the wing to a given $C_{L_{\text{max}}}$ can be solved for, and with equation 6 and the specification of the advance ratio, the required power and torque can be found.

Optimization of the high-lift propeller system pushed towards low propeller diameters, so to keep the results within the range of configurations used to calibrate the model, the fraction of mean slipstream height (equal to $\pi d_p/4$) to mean blown chord, referred to as H/c , was limited (to no less than 0.5). Additionally, the blown span was limited such that the outermost propeller was no farther out than centered on the outer edge of the flap, since blowing the unflapped portion of the wing is less beneficial.

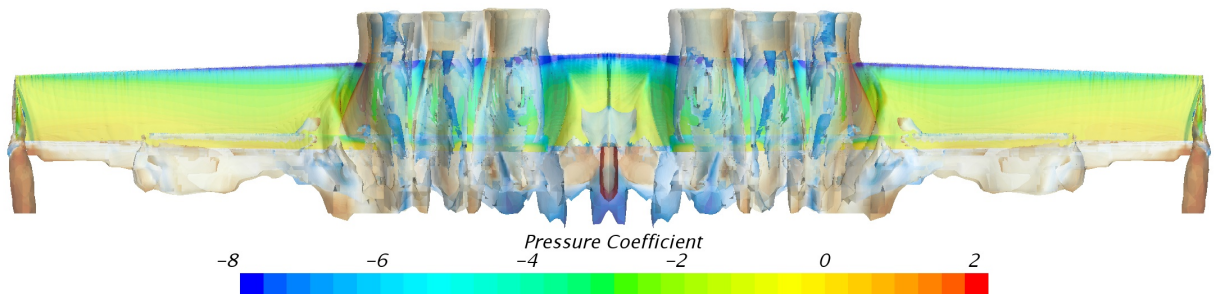


Figure 7. Example of blown wing CFD analyses used to calibrate the analytic blown wing performance model, showing pressure coefficient contours with vorticity isosurfaces. In this case, the $C_{L_{max}}$ is increased from an unblown value of 2.6 to a blown value of 3.9.

Figure 8 illustrates this blown wing model. In figure 8(a), the blown C_L ratio is compared to the slipstream dynamic pressure ratio σ^2 for a range of values of H/c . In an idealized model, the blown C_L ratio would be equal to σ^2 , but finite slipstream effects cause the realized blown C_L ratio to be somewhat less than this ideal value. From this standpoint, blowing a wing is more effective with a larger value of H/c . However, what matters in this application, regardless of how close the blown $C_{L_{max}}$ is to its ideal value, is the weight and drag impact of the high-lift propeller system required to blow the wing. To a first approximation, this is proportional to the sum of the torque requirements of the high-lift propellers. The power required to effect a given dynamic pressure ratio in the slipstream increases roughly linearly with the slipstream height (or the propeller diameter), and, at a fixed tip speed, the torque increases with roughly the square of the slipstream height because the rotation speed decreases with increasing propeller diameter. Figure 8(b) illustrates the sum of motor torque values for a range of values of H/c , and figure 8(c) plots the motor torque requirements versus the blown C_L ratio. Figure 8(c) implies that, for a given blown C_L ratio, a high-lift propeller system will have less impact on weight and drag at lower slipstream heights.

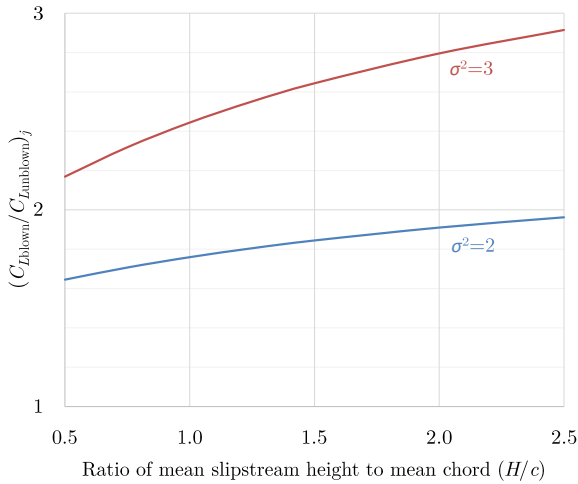
An additional consideration is the amount of thrust the high-lift propeller system produces. If too much thrust is produced, deceleration during approach and landing will be difficult; however, if the propellers are not capable of enough thrust, a tail propeller will be required to trim the aircraft in the event of a wingtip motor loss. Figure 8(d) illustrates the tradeoffs of thrust vs. the sum of motor torque values for a range of values of blown $C_{L_{max}}$ and number of propellers. Generally, meeting the wingtip motor loss trim constraints compromises the design of the aircraft less when accomplished with the high-lift propellers than with an additional tail-mounted motor and propeller. As a result, some designs optimize to a lower number of propellers, in an interesting tradeoff between wingspan (which affects the yaw moment of single wingtip motor operation) and high-lift system weight and drag.

The high-lift propeller system is used during takeoff, approach, and landing segments. The approach segment is flown at $1.3V_{S0}$; the power into the high-lift propellers is that required for a $C_{L_{max}}$ that provides a stall margin of 5 knots (CAS) to the blown stall speed, and the wingtip propellers are utilized as needed to achieve a 3° glide slope. The high-lift motors are sized by determining the power required to meet the specified stall speed at maximum flap deflection at maximum gross weight; the takeoff speed is then calculated by applying this power to the high-lift motors at the takeoff flap setting.

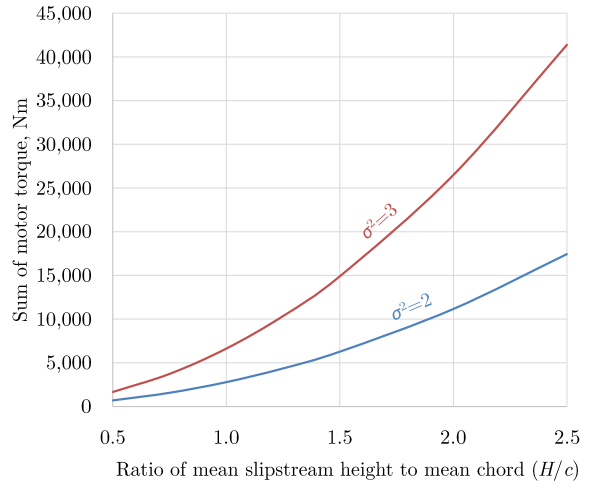
6. One Motor Inoperative Trim Constraints

Federal aviation regulation 14 CFR §23.67 “Climb: One engine inoperative,” part (b) applies to these designs and specifies performance requirements for two conditions.¹⁰ The first of these, §23.67(b)(1), was found to be the limiting of the two:

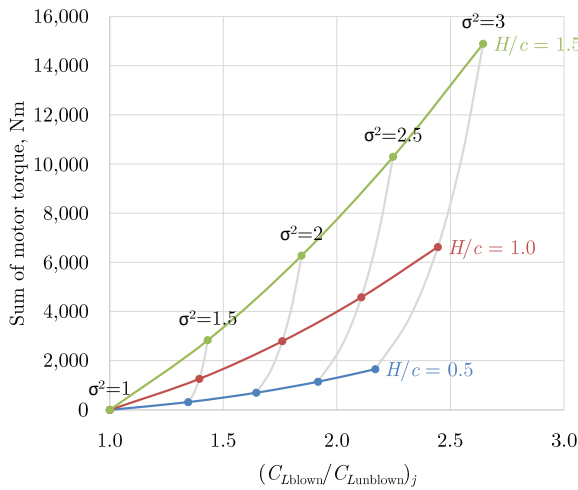
- (1) The steady gradient of climb at an altitude of 400 feet above the takeoff must be no less than 1 percent with the—
 - (i) Critical engine inoperative and its propeller in the minimum drag position;
 - (ii) Remaining engine(s) at not more than maximum continuous power;
 - (iii) Landing gear retracted;
 - (iv) Wing flaps in the takeoff position(s); and
 - (v) Climb speed equal to that achieved at 50 feet in the demonstration of §23.53.



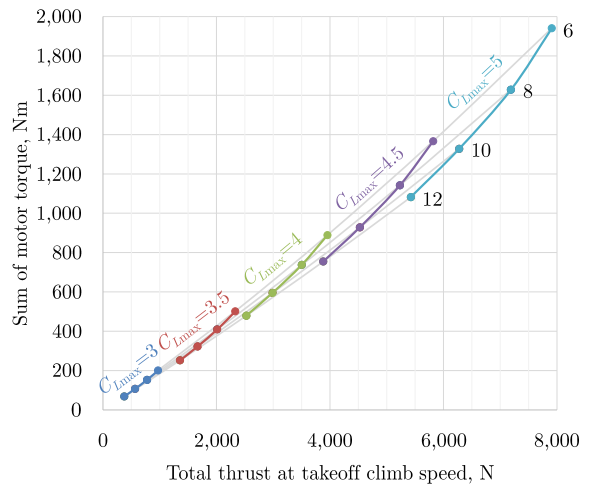
(a) Lift coefficient augmentation vs. slipstream height ($AR_j = 3.7$)



(b) Total torque requirement vs. slipstream height ($AR_j = 3.7$, blown semispan of 4.93 m)



(c) Total torque requirement vs. lift coefficient augmentation ($AR_j = 3.7$, blown semispan of 4.93 m)



(d) Tradeoffs between available thrust and total torque for $H/c = 0.5$ with blown $C_{L_{max}}$ values from 3-5 and high-lift propeller counts from 6-12

Figure 8. Illustration of the blown wing performance model for $V_\infty = 67$ knots and the high-lift propeller parameters given in table 4. σ^2 is equal to the ratio of slipstream to freestream dynamic pressure.

The critical propeller is either of the cruise propellers. The specific conditions chosen to meet this requirement were sea level atmospheric conditions and trimmed flight at a speed of $1.3V_S$ with 20° flap deflection. The inoperative propeller is assumed to be feathered and producing drag according to the feathered prop drag model given by Raymer.¹⁵ To account for the profile drag of the deflected rudder, the vertical tail drag coefficient was increased to 0.041 (relative to the tail area), based on numerical 2D flapped airfoil analyses. The additional induced drag of the vertical tail is calculated assuming a span efficiency of 80% for conventional tails and 100% for T-tails. With an assumed $C_{L_{\max}}$ of 1.0 for the vertical tail, and with the longitudinal center of gravity chosen to meet the specified static margin using the static stability model given by Kroo,¹² the maximum value of thrust the remaining cruise propeller can generate while maintaining yaw trim is calculated by balancing yaw moments. The remaining thrust required to maintain level flight must then be provided by the tail propeller and/or the high-lift propellers.

Additionally, §23.66 specifies that the aircraft must be able to be trimmed at the same speed as above with “the critical engine inoperative” and “the remaining engine(s) at takeoff power;” this serves as a constraint on vertical tail sizing.

B. Weight Models

The wing weight estimate is calculated as a sum of a term proportional to the maximum bending stress and a term proportional to wetted wing area, in a similar manner to various published models.^{12,19} However, the bending term is assumed to be proportional to the sum of a fixed constant and the inverse of the specific strength of the material, instead of a scaling factor applied to the inverse of the specific strength of the material. This allows the model to more accurately describe both traditional metal wings and carbon fiber composite wings, because the mass benefit of composite construction will mostly be realized in the portion of the wing that directly resists bending stresses (e.g. the spar), since the fibers can be very efficiently oriented in this portion of the structure. This model therefore provides a conservative approximation of the weight savings of carbon fiber construction relative to metal construction.

The two free parameters of this model were obtained by regression against similar aircraft with known wing masses (Cessna 310,²⁰ Cessna 404,²⁰ and Tecnam P2006T²¹), assuming a specific strength corresponding to 7075-T6 aluminum values of $\rho_{\text{wing,Al}} = 2,810 \text{ kg/m}^3$ and an allowable stress of $\sigma_{\text{allow,Al}} = 503 \text{ MPa}$.²² The calibrated wing mass equation is

$$m_{\text{wing}} = \left(0.56 \frac{\rho_{\text{wing,Al}}}{\sigma_{\text{allow,Al}}} + \frac{\rho_{\text{wing}}}{\sigma_{\text{allow}}} \right) \frac{b^3 N_z W}{8S(\frac{5}{6}t/c) \cos^2 \Lambda} \frac{2}{3} \frac{1 + 2\lambda}{1 + \lambda} + (3.60 \text{ kg/m}^2) S_{\text{wet}} \quad (10)$$

where the wetted area is calculated by equation 4. The first term, which is proportional to bending stresses, is therefore 56% greater than the ideal minimum in the case of an aluminum wing, and a larger amount above the ideal minimum for carbon fiber. Material properties assumed for carbon fiber composites are $\rho_{\text{wing}} = 1,700 \text{ kg/m}^3$ and $\sigma_{\text{allow}} = 700 \text{ MPa}$. Example results from this model are shown in figure 9, along with the statistical general aviation metal construction wing weight model from Raymer¹⁵ for comparison.

Weight models for the fuselage, tails, anti-ice system, flight controls, and fuel system are those proposed by Raymer¹⁵ for general aviation aircraft. The installed engine weight is assumed to be 120% of the dry uninstalled engine weight.

The mass of each motor is given by the relation kQ/d_m , where d_m is the motor diameter and Q is the maximum continuous motor torque. The constant k is taken as 0.036 kg-m/Nm for the wingtip and tail motors, which are direct-drive for simplicity and reliability. The high-lift motors are geared to save

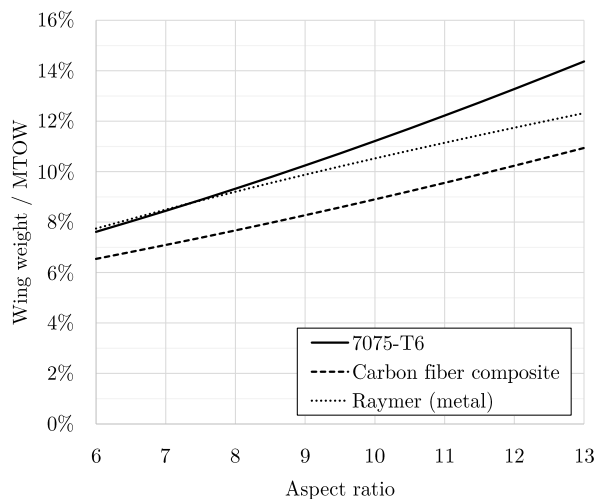


Figure 9. Wing weight model examples for varying aspect ratio for a fixed wing area ($W = 7,610 \text{ lb}$, $S = 274 \text{ ft}^2$, $N_z = 5.25$, $\lambda = 0.72$, $t/c = 16\%$)

weight, and the combined motor and gearbox weight follows this model with a k value of 0.010 kg-m/Nm. With the motor diameter as a design variable, the tradeoff between motor mass and nacelle drag (which is proportional to motor diameter) can then be explored. Motor controllers are assumed to have a specific power of 20 kW/kg. A specific energy of 400 Wh/kg is assumed for the battery packs.

The propeller weights follow the model proposed by Plencner et al.,²³ scaled to match the weight of the contemporary carbon fiber MTV-7 propeller (including hub).²⁴ The folding propellers are fixed-pitch, and because it was assumed that the weight of the associated folding mechanism is equal to the weight of the equivalent variable-pitch hub estimated by this model, no modifications of this model were required for such applications.

Based on a figure from the Cessna 402, the air conditioning system is assumed to add 36 kg.²⁵ Avionics and avionics hardware were assumed to add 38 kg, and cabin furnishings were assumed to add 180 kg.

Finally, the empty weight was increased by 5% to account for weight growth and inaccuracies. This additional weight is categorized as “miscellaneous.”

Example weight breakdowns are shown in figure 10. Note that, even though the battery-only range is only 100 nm, the battery weight drives the empty weight of the hybrid electric designs to a much higher value than the conventional design, despite the weight savings imparted by the smaller engines (since the battery can provide some of the required power).

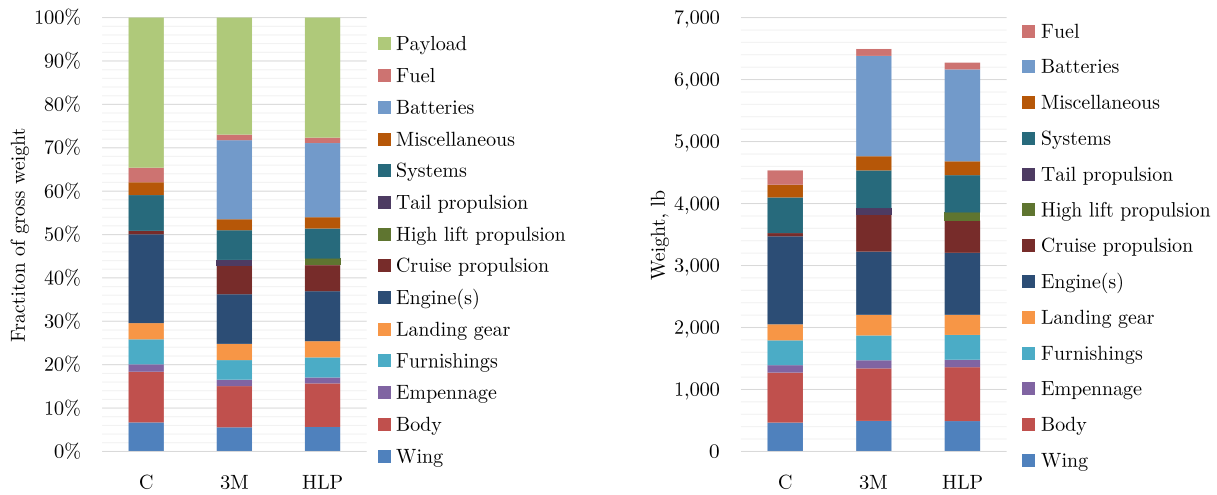


Figure 10. Weight breakdown examples for turbodiesel designs, $V_{400} = 225$ knots

C. Powertrain Models

Three different rubber engine models were considered: a turbocharged diesel (turbodiesel), a turboprop, and an advanced recuperated turbine generator (turbogenerator). The relevant specifications for these are given in table 5, along with the assumed operating specifications for the engines of the reference aircraft. The specific fuel consumption is assumed constant except for the case of the turbodiesel, which is plotted in figure 11. The turbodiesel specifications are based off those of the SMA SR305,^{26,27} and the turboprop specifications are based off smaller variants of the popular PT6A family, such as the PT6A-21.²⁸⁻³¹

Engine shaft power lapse with altitude is modeled as³²

$$\frac{P_{A,\text{turbine}}}{P_{A,0}} = \left(\frac{\rho}{\rho_0}\right)^{0.7} \quad (11)$$

$$\frac{P_{A,\text{piston}}}{P_{A,0}} = 1.132 \left(\frac{\rho}{\rho_0}\right) - 0.132 \quad (12)$$

where ρ_0 and $P_{A,0}$ are the air density and maximum shaft power output at the critical altitude and $P_A = P_{A,0}$ below the critical altitude.

Table 5. Engine model assumptions

	Turbodiesel	Turboprop	Turbogenerator	C402	P2012	PC-12
SFC*(75% power), g/kWh	219	383	274	281	252	309
Time between overhaul, hours	2,400	3,600	6,000	2,700	2,000	3,500
Critical altitude, ft	10,000	Sea level	Sea level	16,000	10,000	18,000
Specific power, kW/kg	0.79	3.5	3.4			
Unit cost per kW	\$530	\$750	\$750			
Overhaul cost per kW [†]	\$340	\$560	\$560	\$160	\$150	\$520
Minimum size (P_{\min}), kW	170	185	185			

* Specific fuel consumption

[†] Includes prorated hot section inspection cost, if applicable

The combined motor and controller efficiency assumptions are 95% for the generator and high-lift motors and 96% for the wingtip and tail motors.

The size (maximum power) of each motor is determined by the maximum power requirement throughout the design missions, including the motor loss conditions described previously. Total takeoff power is estimated by a statistical method for predicting the FAR 23 takeoff distance of propeller-driven airplanes from hard-surface runways.³³ On the distributed propulsion designs, this power is divided between all of the motors, with the wingtip motors producing any remaining power if the combination of the other motors is not powerful enough. This means that the takeoff power requirement has the potential to drive the size of the wingtip motors, but not any of the other motors.

D. Cost Models

The purchase cost of the aircraft is estimated using the model from Eastlake and Blackwell³⁴ as described by Gudmundsson,³⁵ with wrap rates inflation-adjusted to \$95, \$63, and \$55 per hour for engineering, tooling, and manufacturing, respectively. The business aircraft model was employed, because it produced a more realistic price estimate than the general aviation model when applied to the Tecnam P2012, and no particular development or certification cost penalties are applied to the electric aircraft, since it is assumed that these costs will be relieved by government investment in such technology. A 5-year production quantity of 500 aircraft is assumed. Avionics are assumed to cost \$60,000. Electric propulsion system component costs are summarized in table 6; only the high-lift propeller motors are geared.

Table 6. Electric propulsion component costs

Motor	Geared motor	Motor controller	Generator
\$50/kW	\$100/kW	\$100/kW	\$200/kW

Examples results from this cost model are illustrated in figure 12.

The operating costs are assumed to be the sum of the following components:

- Battery amortization: The batteries last for 2,000 cycles, after which they must be replaced at a cost of 20¢/Wh, based on published battery pack cost projections.³⁶ One cycle is defined to be a cumulative discharge of 80% of the battery capacity.

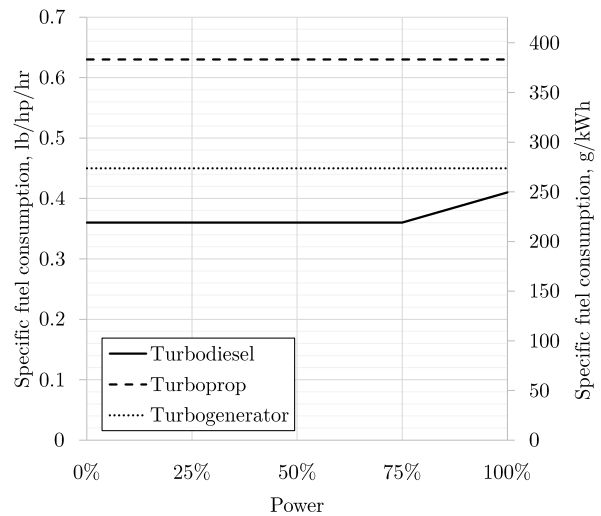


Figure 11. Specific fuel consumption models

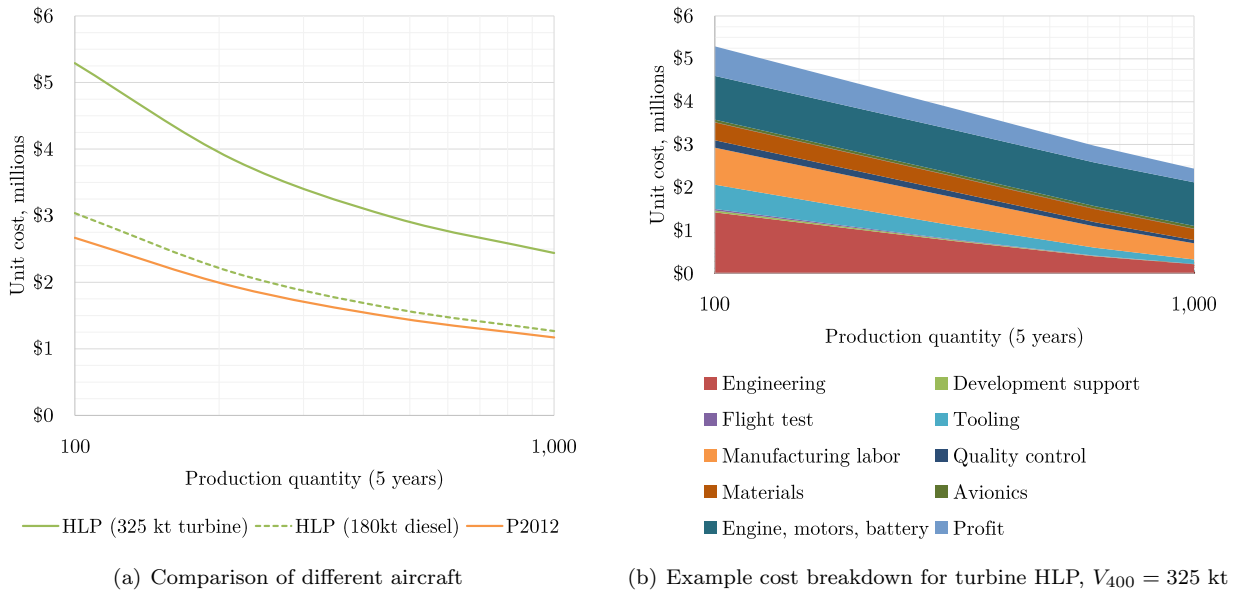


Figure 12. Example results of the cost model for a range of production quantities

- Electricity cost: 7¢/kWh (a typical industrial rate). An assumed charging efficiency of 95% results in an effective cost about 5% higher than this.
- Overhaul: The cumulative time an engine is running during a flight counts towards its engine time, and the overhaul is performed at 95% of the rated time between overhauls.
- Fuel: \$3.50/gallon for diesel, avgas, and Jet A.
- Depreciation: Depreciation is over 30,000 flight hours. Electric aircraft operations require a charging station, which is assumed to cost \$300,000 and depreciate over 100,000 flight hours.
- Interest: 6% of the purchase price per year, with a utilization of 1,500 flight hours per year.
- Pilot: \$40/hour. This rate applies to the flight time plus 40 minutes, to account for time on the clock between flights.
- Maintenance: This comprises all maintenance costs aside from the engine overhaul, and is described for different aircraft types in table 7.
- Insurance: \$1.60 per million dollars of aircraft purchase cost plus \$4.70 per flight, based off figures from Cape Air.³⁷
- Landing fees: \$4 per 1,000 lb of MTOW.³⁷

Table 7. Maintenance cost per flight hour assumptions

Advanced concepts	Cessna 402	Tecnam P2012	Pilatus PC-12
\$140 [*] / \$105 [†]	\$238 ³⁷	\$120 ¹	\$140 [‡]

^{*} Flights utilizing combustion engine(s)

[†] Fully-electric flights: 25% lower, assuming that 50% of the baseline maintenance costs are related to the propulsion system, and this portion is reduced by 50% when the combustion engine is not operated

[‡] Adjusted from the value given by Pilatus³⁸ to reflect the estimated labor rate difference between executive and commercial operation

Operating cost figures for the reference aircraft are a combination of data published by Cape Air,¹ Tecnam,⁴ and Pilatus,³⁸ and, where no data was available, the authors' best estimates. All cost figures are inflation-adjusted to 2015 dollars. Example operating cost breakdowns are shown in figures 13 and 14. (Figures 13(a) and 14 present the same data in different formats.)

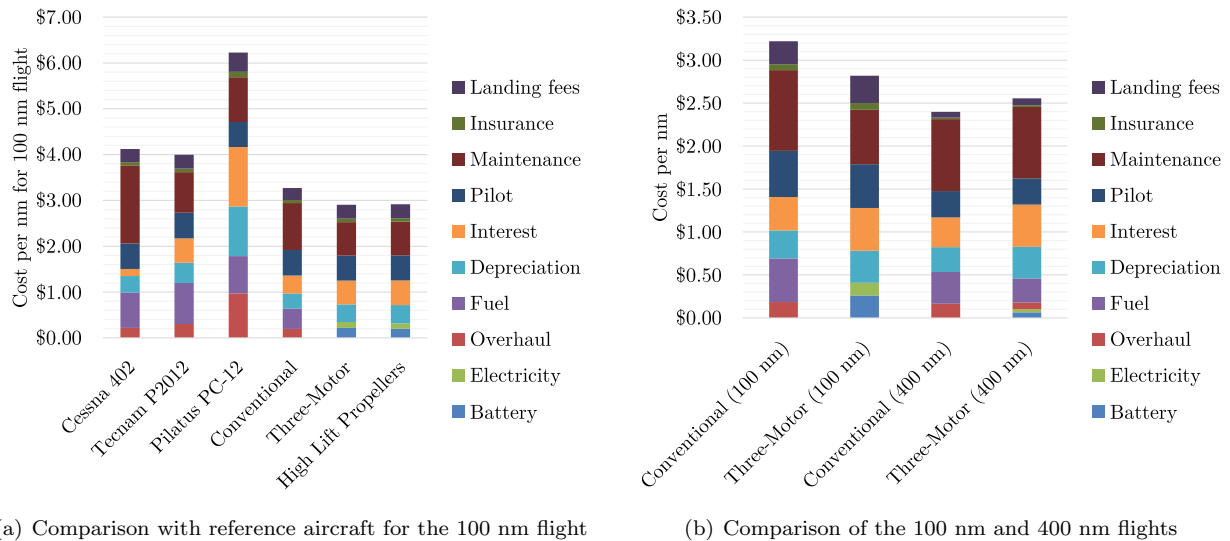


Figure 13. Operating cost estimates of the turbodiesel advanced concepts for the 100 nm flight for $V_{100} = V_{400} = 180$ knots

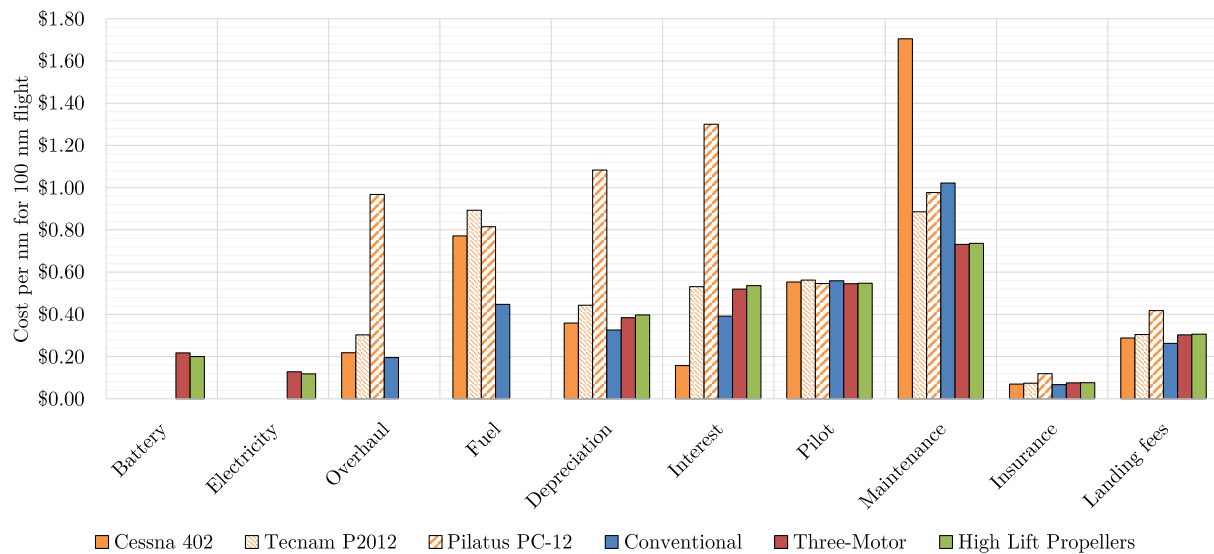


Figure 14. Operating cost estimates of the turbodiesel advanced concepts and the reference aircraft for $V_{100} = V_{400} = 180$ knots

Figure 13(b) compares the operating costs of the conventional and three-motor concepts for the 100 nm and 400 nm flights. For the 100 nm flight, because the battery and electricity costs of the three-motor design are significantly lower than the fuel and overhaul costs of the conventional design, the three-motor design is less expensive overall despite its disadvantage in interest and depreciation costs. However, for the 400 nm flight, the advantage in battery, electricity, fuel, and overhaul costs is too small to balance out the disadvantage in interest and depreciation costs, so the conventional design is less expensive overall.



Figure 15. The $V_{400} = 275$ KTAS optimized advanced concepts and the reference aircraft the same scale

Table 8. Comparison of turbodiesel-powered advanced concepts for $V_{400} = 180$ knots with reference aircraft

	C402	P2012	PC-12	C	3M	HLP
Max takeoff weight (lb)	7,210	7,610	10,450	6,652	7,930	7,729
Wing area (ft ²)	226	274	278	168	201	161
Wing loading (lb/ft ²)	31.9	27.8	37.6	39.5	39.5	47.9
Wingspan (ft)	44.1	44.5	53.2	46.3	38.1	43.6
Aspect ratio	8.6	7.2	10.2	12.7	7.2	11.9
Fuel capacity (gal)	213	164	402	57	46	44
Battery size (kWh)	-	-	-	-	262	231
Engine power (kW)	485	522	895	370	173	169
Cruise power*, 400 nm flight (kW)	327	429	276	250	249	233
$C_{L_{max}}$	2.1	2.3	2.5	2.6	2.6	3.2
Unit cost (million)	\$0.55 ¹	\$1.8 [†]	\$4.7 ³⁹	\$1.5	\$1.8	\$1.8
Weighted mission cost/nm	\$3.87	\$3.74	\$5.84	\$3.01	\$2.76	\$2.77

* Power from the engine(s) and/or batteries

† Estimated

V. Results

Table 8 details selected attributes of exemplary optimized advanced concept designs compared with the reference aircraft, and figure 15 illustrates the optimal designs for $V_{400} = 275$ KTAS along with the reference aircraft at the same scale. The reduction in maximum range coupled with higher wing loading and composite construction of the advanced concepts results in a significant weight advantage relative to the reference aircraft; combined with the fuel-efficient turbodiesel, the mission costs are also reduced significantly.

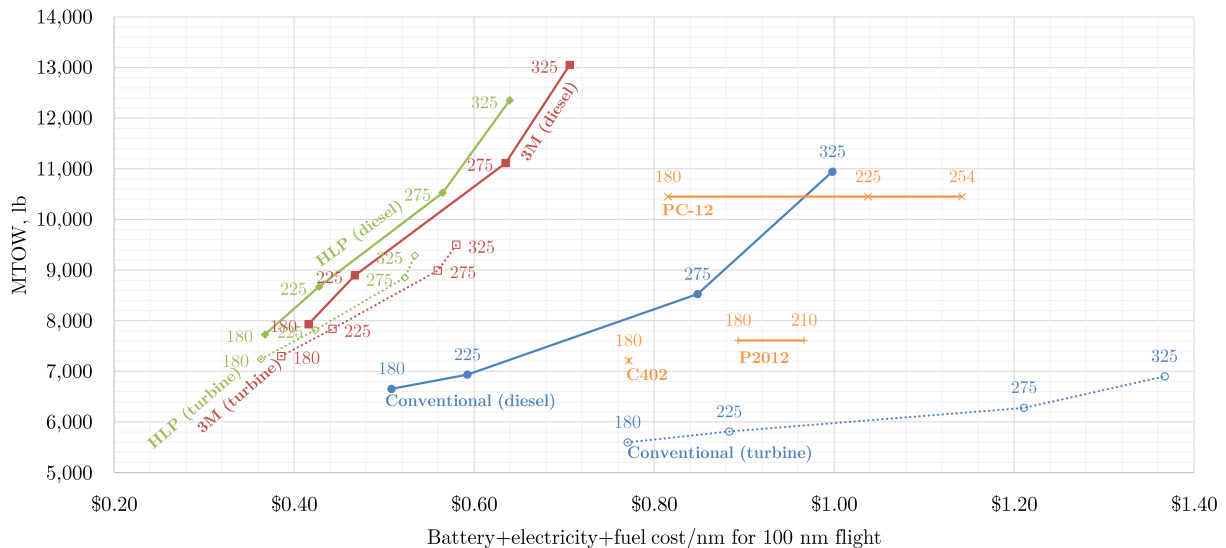


Figure 16. Energy cost vs. weight for advanced concept designs at values of V_{400} from 180 kt to 325 kt, compared to reference aircraft at various cruise speeds (indicated by the data labels)

Figure 16 compares the sum of the battery, electricity, and fuel costs with the maximum takeoff weight of a series of optimized advanced concept designs for a range of values of V_{400} with the reference aircraft operated at comparable speeds. The electric aircraft are lower in battery+energy+fuel costs, but are heavier, so it is difficult to assess how attractive these designs are compared to the conventional designs by these

metrics alone.

Figure 17 illustrates the results of the optimization with a series of plots. In figure 17(a), the weighted total cost per nm is plotted as a function of the cruise speed for the 400 nm flight, V_{400} . At every choice of V_{400} , the advanced concepts are lower-cost than the reference aircraft, and the electric propulsion configurations are lower-cost than the conventional configurations. The high-lift propellers (HLP) configuration is similar in cost to the three-motor (3M) configuration at lower speeds, but gradually becomes more competitive as the speed is increased. This is as expected, since the potential of the high-lift propellers configuration to achieve higher wing loadings is more beneficial at higher speeds. Whereas the operating costs of the turboprop-powered conventional configuration are higher than the turbodiesel-powered conventional configurations, the versions of the electric propulsion configurations utilizing the advanced recuperated turbine generator achieve better operating costs than the respective turbodiesel-powered designs at higher speeds, where the higher power requirements favor engines with better specific power. Also, as expected, the costs increase for all three configurations as the design speeds are increased.

Whereas the operating costs of electric propulsion designs decrease monotonically with V_{400} , the operating costs for the conventional designs level out between $V_{400} = 225$ KTAS and $V_{400} = 180$ KTAS. This is because, at $V_{400} = 180$ KTAS, the optimal cruise speed for the 100 nm mission, V_{100} , is greater than V_{400} (as seen in figure 17(b)), and the power requirements needed to reach this speed are more burdensome for the conventional designs than the hybrid designs, since the hybrid designs do not need to increase the size of the combustion engine(s) to reach this higher speed.

Figure 17(b) compares the optimized value of the cruise speed for the 100 nm flight, V_{100} , with the choice of speed for the 400 nm flight, V_{400} . For all configurations, $V_{100} > V_{400}$ at lower values of V_{400} and $V_{100} \leq V_{400}$ at higher values of V_{400} . At $V_{400} = 325$ KTAS, the conventional designs cruise at $V_{100} = V_{400}$, but the hybrid designs cruise at a significantly lower value of V_{100} . This is because the optimized hybrid designs cruise at a higher altitude in the 400 nm flight (and therefore at a lower calibrated airspeed), while the conventional designs cruise at 10,000 feet.

Figures 17(c) and 17(d) show the total costs for the 100 nm and 400 nm flights. The electric designs fare relatively better compared to the conventional designs in the 100 nm flight, in which they are running fully electric, than the 400 nm flight, in which they are still compromised on weight due to the battery packs but must run the range extender.

Figure 17(e) shows that the sensitivity of the weighted cost to increasing battery pack energy density from 400 Wh/kg to 500 Wh/kg is relatively small.

Figure 17(f) shows the total combined power of the combustion engine(s) for each design. All the advanced concepts, being designed for a higher wing loading and lower maximum range, require less power than the reference designs, and the electric designs require less power than the conventional designs due to the ability to supplement the engine power with batteries.

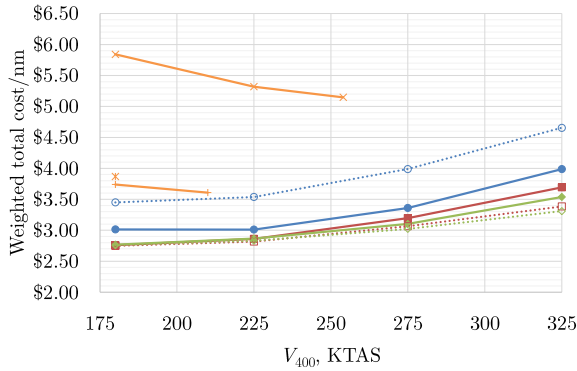
Figure 18 shows the sensitivity of operating costs to fuel and electricity costs. The baseline designs are analyzed at the baseline costs and at an alternate scenario with higher costs. Because the electricity cost is a relatively small portion of operating costs compared to fuel costs (as illustrated by figure 13(a)), increased electricity cost has a smaller impact on total operating costs than increased fuel cost. As a result, whereas the volatile fuel costs typically seen in the airline industry can present strategic difficulties for airlines due to uncertain future operating costs, volatile electricity costs will have a much weaker effect. Even for the 400 nm flight (figure 18(b)), where the hybrid designs are burning fuel, the use of batteries as well reduces the relative change in operating costs, increasing the attractiveness of these designs relative to the conventional designs compared to the baseline scenario.

Exemplary power profiles for both flights are illustrated in figure 19. The reduction in engine size required for cruise power is evident, since the battery provides a portion of the power in flight segments where the generator alone is insufficient.

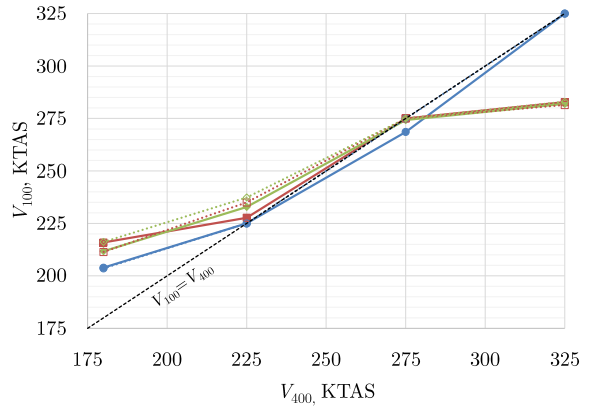
Figures 20(a) and 20(b) show the resultant MTOW and wing aspect ratio, respectively, for each optimized design. The impact of the greater specific power of the turbine powerplants relative to the diesels on MTOW is apparent, as is the weight penalty on the electric aircraft of carrying batteries.

Figures 20(c) and 20(d) illustrates the significant increase in wing loading and $C_{L_{max}}$ possible with the high-lift propeller system, and how this scales with design speed (V_{400}); as expected, higher design speeds result in higher optimal values of wing loading.

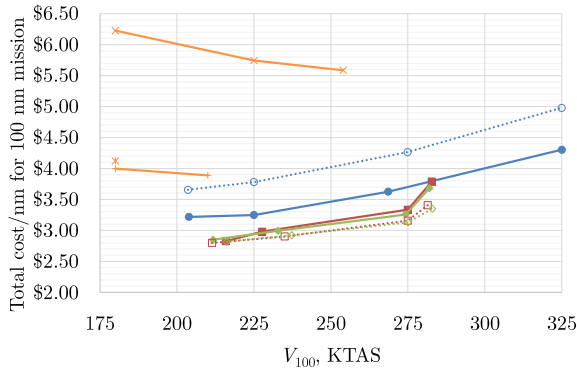
As seen from figure 17(a) (and more apparent in figure 17(e) due to the tighter scale), although the high-lift propeller configuration presents a lower operating cost than the three-motor configuration for most



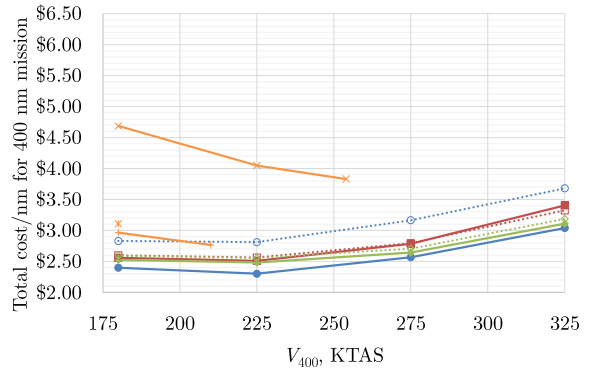
(a) Weighted costs



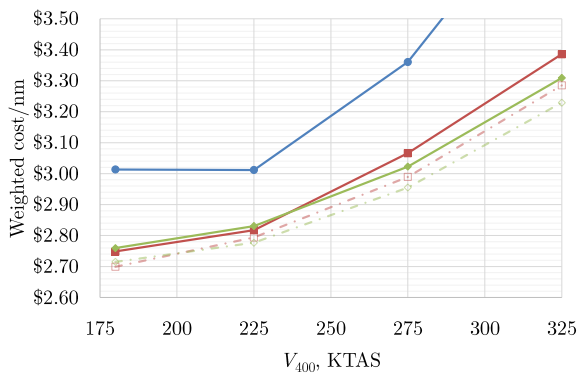
(b) Optimized values of V_{100}



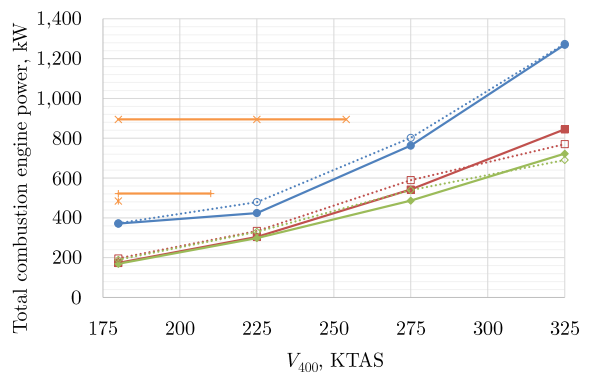
(c) 100 nm flight costs at V_{100}



(d) 400 nm flight costs at V_{400}



(e) Effect of specific energy on operating cost



(f) Engine power as function of V_{400}

Figure 17. Optimization results

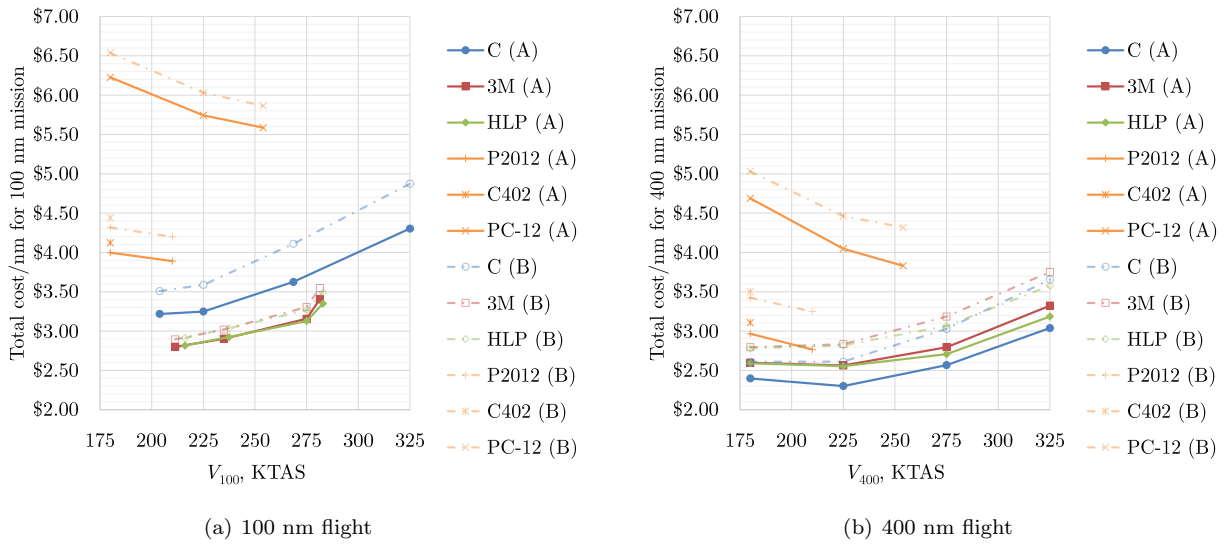


Figure 18. Total operating costs for two scenarios: (A) fuel is \$3.50/gal and electricity is 7¢/kWh; (B) fuel is \$5.50/gal and electricity is 12¢/kWh

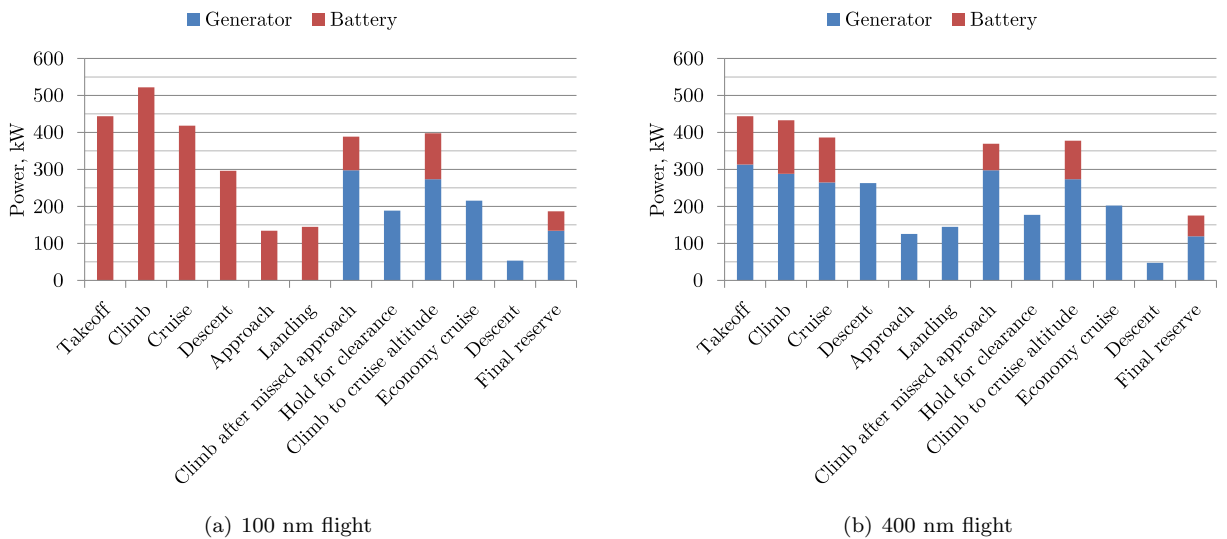


Figure 19. Mission power profiles for the turbogenerator high-lift propellers configuration at $V_{400} = 225$ KTAS

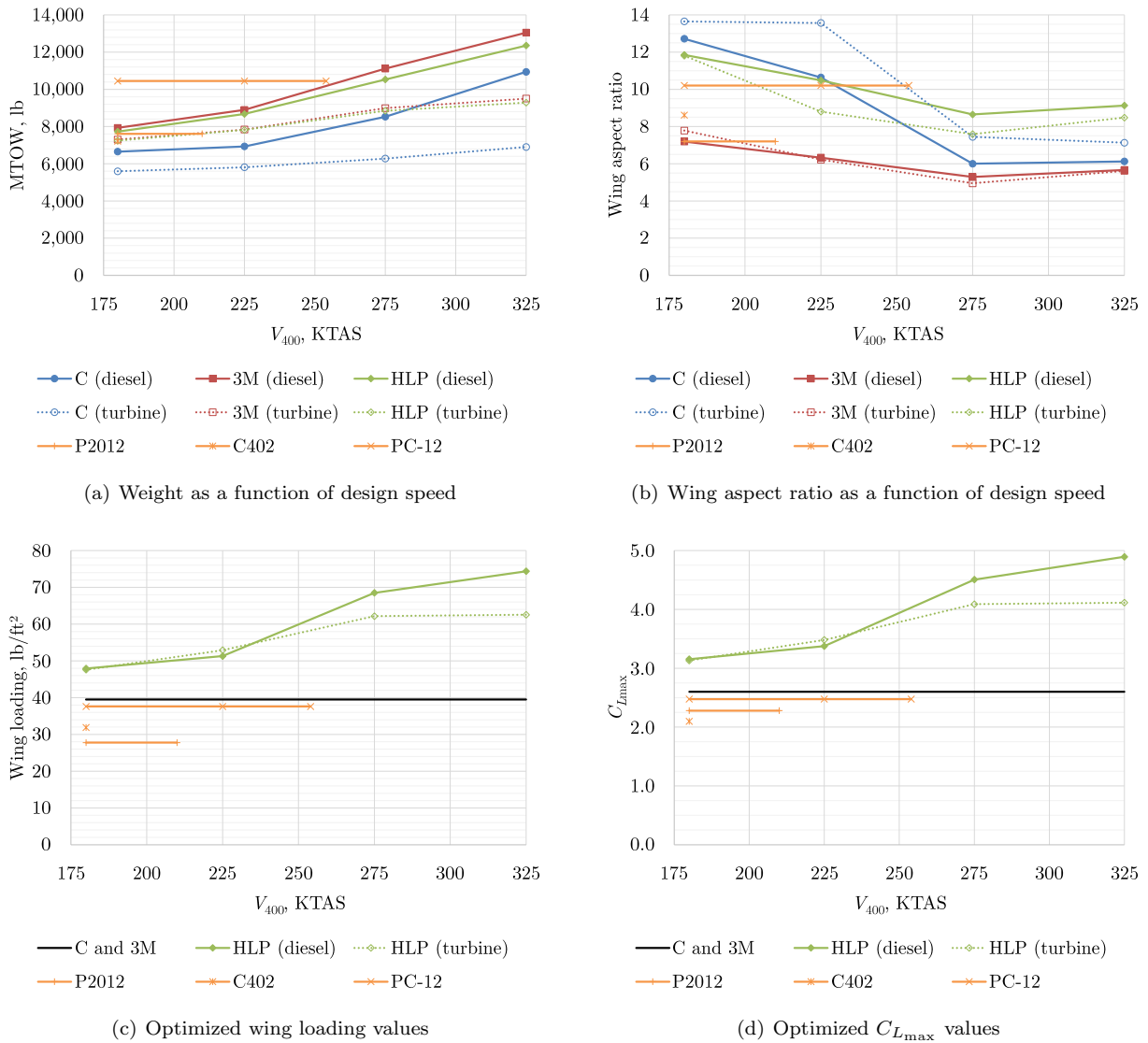


Figure 20. Optimized values of design parameters

values of V_{400} , the difference is small. This is because, although the wing parasitic drag is greatly decreased due to the higher wing loading, this drag only comprises a fraction of the total drag, and although the horizontal tail area can be reduced as well, the lift-dependent drag typically increases due to higher span loading. Therefore, the reduction of total drag is relatively less significant. This drag reduction results in lower battery, energy, fuel, and overhaul costs, but, particularly for the 100 nm flight, these costs comprise a relatively small fraction of the total operating cost. The remaining components of the total operating cost do not change much, so the impact on total operating cost is relatively minor.

Considering the case of the three-motor and high-lift propeller designs on the 100 nm mission for $V_{400} = 325$ knots with the turbogenerator range extender as an example, at the cruise condition the wing parasitic drag decreases from 1,149 N (27% of total cruise drag) to 807 N—a 30% reduction—and the lift-dependent drag increases from 401 N to 455 N; the total cruise drag decrease is 8%. The sum of the mission battery and energy costs decreases by 8% (as seen in figure 16), but this quantity comprised only 17% of total operating costs, which are then reduced by only 1.6%. The differences are slightly larger for the 400 nm mission at higher design speeds (compare figures 17(c) and 17(d)), because the reductions of fuel and overhaul costs due to lower cruise drag impact the total operating costs to a larger extent than reductions in battery and energy costs.

VI. Conclusion

Although significant savings in energy costs can be attained in such aircraft, the savings in total operating costs are reduced somewhat by increased depreciation and interest costs driven by the larger aircraft size required to carry enough batteries to perform a significant flight on batteries only. Increased battery energy density from 400 Wh/kg to 500 Wh/kg does not significantly change this tradeoff. This result does not necessarily imply certain limits on the benefits of electric propulsion to thin haul aircraft designs, because it may be the case that the configurations chosen for this study are not the best configurations for this mission. (For example, perhaps parallel hybrid configurations would be better-suited.) Alternatively, the chosen missions may not be optimal for the configurations presented here: further investigations may reveal different design missions that are better suited to these aircraft.

However, the electric aircraft designs of this study still attain lower operating costs than the equivalent conventional aircraft designs. This cost advantage increases as the design cruise speeds are increased, demonstrating the relative attractiveness of electric propulsion for higher-speed aircraft designs, since the higher power requirements are less compromising due to the higher specific power of the propulsion system. Among the two electric configurations studied, the high-lift propellers configuration presents an operating cost advantage in most cases, most notably at high design speeds with the turbodiesel range extender option. In addition to these cost savings, the electric designs are also expected to significantly improve on conventional designs in noise and emissions.

VII. Acknowledgments

The authors would like to thank Mark Moore, Dr. Michael Patterson, Ken Goodrich, Bill Fredericks, and Dr. Nick Borer at NASA Langley Research Center, and JoeBen Bevirt at Joby Aviation, for their support and mentorship through the course of this project. Additionally, the authors would like to thank Dr. Joachim Grenestedt for his advice on structural modeling, and Cape Air for their aid in providing insight into operational considerations of such aircraft. Funding support was provided for this research by NASA Langley Research Center through the On-Demand Mobility exploratory studies, as part of the Transformational Aviation Concepts Program.

References

- ¹Wolf, D. A., “Commuter Airline Perspective,” presented at the On-Demand Mobility and Emerging Technology Joint NASA-FAA Workshop, Arlington, VA, March 2016.
- ²Cessna Aircraft Company, *1980 Model 402C Information Manual*, 4th ed., December 2012.
- ³“Cessna 402C Limitations/Systems Review Guide,” Cape Air, November 2005, Revision #1.
- ⁴“Competitors Comparison — P2012 Traveler,” <http://p2012.tecnam.org/competitors-comparison/>, Accessed: 2016-03-08.
- ⁵“Cabin — P2012 Traveler,” <http://p2012.tecnam.org/images/cabin/>, Accessed: 2016-03-08.
- ⁶Pilatus, *PC-12 Pilot’s Information Manual*, 14th ed., December 2014.
- ⁷Moore, M. D. and Fredericks, W. J., “Misconceptions of Electric Propulsion Aircraft and Their Emergent Aviation Markets,” *The 52nd Aerospace Sciences Meeting AIAA SciTech*, American Institute of Aeronautics and Astronautics, January 2014.
- ⁸Miranda, L. and Brennan, J., “Aerodynamic Effects of Wingtip-Mounted Propellers and Turbines,” *Fluid Dynamics and Co-located Conferences*, American Institute of Aeronautics and Astronautics, June 1986.
- ⁹Stoll, A. M., Bevirt, J., Moore, M. D., Fredericks, W. J., and Borer, N. K., “Drag Reduction Through Distributed Electric Propulsion,” *14th AIAA Aviation Technology, Integration and Operations Conference*, American Institute of Aeronautics and Astronautics, June 2014.
- ¹⁰Office of the Federal Register (United States), *Code of Federal Regulations, Title 14*, 2016.
- ¹¹Morris, J. and Ashford, D. M., “Fuselage Configuration Studies,” Technical Paper 670370, SAE, February 1967.
- ¹²Kroo, I., “Aircraft Design: Synthesis and Analysis,” <http://adg.stanford.edu/aa241/aircraftdesign.html>.
- ¹³Cavallo, B., “Subsonic Drag Estimation Methods,” Tech. Rep. NADC-AW-6604, US Naval Air Development Center, 1966.
- ¹⁴Costruzioni Aeronautiche Tecnam, *P2006T - Aircraft Flight Manual*, 3rd ed., March 2014.
- ¹⁵Raymer, D. P., *Aircraft Design: A Conceptual Approach*, American Institute of Aeronautics and Astronautics, Inc., 4th ed., 2006.
- ¹⁶Stoll, A. M., Bevirt, J., Pei, P. P., and Stilson, E. V., “Conceptual Design of the Joby S2 Electric VTOL PAV,” *14th AIAA Aviation Technology, Integration, and Operations Conference*, American Institute of Aeronautics and Astronautics, June 2014.
- ¹⁷Phillips, W. F., *Mechanics of Flight*, John Wiley & Sons, Ltd, 2004.

- ¹⁸Jameson, A., “Preliminary Investigation of the Lift of a Wing in an Elliptic Slipstream,” Aerodynamics Report 393-68-6, Grumman, 1968.
- ¹⁹Grenestedt, J. L. and Spletzer, J. R., “Towards Perpetual Flight of a Gliding Unmanned Aerial Vehicle in the Jet Stream,” *49th IEEE Conference on Decision and Control (CDC)*, Dec 2010, pp. 6343–6349.
- ²⁰Sadraey, M. H., *Aircraft Design: A Systems Engineering Approach*, John Wiley & Sons, Ltd, 2013.
- ²¹Russo, F., “Aircraft P2006 T Weight & Balance Analysis - Garmin G950,” Rev. 1 2006/256, Costruzioni Aeronautiche Tecnam, March 2010.
- ²²“ASM Material Data Sheet: Aluminum 7075-T6; 7075-T651,” <http://asm.matweb.com/search/SpecificMaterial.asp?bassnum=MA7075T6>.
- ²³Plencner, R., Senty, P., and Wickenheiser, T., “Propeller Performance and Weight Predictions Appended to the Navy/NASA Engine Program,” Technical Memorandum NASA-TM-83458, NASA, Lewis Research Center, Cleveland, Ohio, August 1983.
- ²⁴MT-Propeller Entwicklung GmbH, *MTV-7-() Variable Pitch Propeller*, March 2005.
- ²⁵Cook, L., “The Cessna 402: A Versatile Cabin-Class Twin,” *Twin & Turbine*, Vol. 19, No. 10, October 2015.
- ²⁶“Cessna Skylane JT-A International Brochure,” Cessna Aircraft Company, 2013.
- ²⁷“SMA: Plans For SR305 Diesel,” *AVweb flash*, July 2004, <http://www.avweb.com/avwebflash/leadnews/187815-1.html>.
- ²⁸“Civil Turboshift/Turboprop Specifications,” <http://www.jet-engine.net/civtsspec.html>.
- ²⁹“Recommended Service Intervals,” Airforce Turbine Service, Ltd., 2010.
- ³⁰“Financial Analysis of the King Air C90A with the Blackhawk XPR135A Engine Upgrade,” Blackhawk Modifications, Inc., August 2009.
- ³¹“PT6 Engine Models,” <http://www.iascanada.com/engmodels.html>.
- ³²Anderson, J., *Aircraft Performance & Design*, McGraw-Hill Education, 1998.
- ³³Roskam, J. and Lan, C.-T. E., *Airplane Aerodynamics and Performance*, Design, Analysis and Research Corporation, 1st ed., 1997.
- ³⁴Eastlake, C. N. and Blackwell, H. W., “Cost Estimating Software for General Aviation Aircraft Design,” *Proceedings of the ASEE National Conference*, St. Louis, MO, 2000.
- ³⁵Gudmundsson, S., *General Aviation Aircraft Design: Applied Methods and Procedures*, Butterworth-Heinemann, 1st ed., 2013.
- ³⁶Hensley, R., Newman, J., and Rogers, M., “Battery Technology Charges Ahead,” *McKinsey Quarterly*, July 2012.
- ³⁷“Cape Air Cessna 402 cost model,” Cape Air, September 2014.
- ³⁸“PC-12 NG Just The Facts,” Pilatus Aircraft Ltd, 2016.
- ³⁹Goyer, R., “PC-12 Versus the World,” *Flying*, July 2013.